

FERENGI: REDSHIFTING GALAXIES FROM SDSS TO GEMS, STAGES AND COSMOS

M. BARDEN^{1,2}, K. JAHNKE¹, B. HÄUSSLER¹

Accepted September 26, 2007 to ApJL

ABSTRACT

We describe the creation of a set of artificially “redshifted” galaxies in the range $0.1 < z < 1.1$ using a set of ~ 100 SDSS low redshift ($v < 7000 \text{ km s}^{-1}$) images as input. The intention is to generate a training set of realistic images of galaxies of diverse morphologies and a large range of redshifts for the GEMS and COSMOS galaxy evolution projects. This training set allows other studies to investigate and quantify the effects of cosmological redshift on the determination of galaxy morphologies, distortions and other galaxy properties that are potentially sensitive to resolution, surface brightness and bandpass issues. We use galaxy images from the SDSS in the u, g, r, i, z filter bands as input, and computed new galaxy images from these data, resembling the same galaxies as located at redshifts $0.1 < z < 1.1$ and viewed with the Hubble Space Telescope Advanced Camera for Surveys (HST ACS). In this process we take into account angular size change, cosmological surface brightness dimming, and spectral change. The latter is achieved by interpolating a spectral energy distribution that is fit to the input images on a pixel-to-pixel basis. The output images are created for the specific HST ACS point spread function and the filters used for GEMS (F606W and F850LP) and COSMOS (F814W). All images are binned onto the desired pixel grids ($0''.03$ for GEMS and $0''.05$ for COSMOS) and corrected to an appropriate point spread function. Noise is added corresponding to the data quality of the two projects and the images are added onto empty sky pieces of real data images. We make these datasets available from our website, as well as the code – FERENGI: “Full and Efficient Redshifting of Ensembles of Nearby Galaxy Images” – to produce datasets for other redshifts and/or instruments.

Subject headings: galaxies: high-redshift – galaxies: structure – galaxies: fundamental parameters

1. INTRODUCTION

In the current era of observational astronomy the size of galaxy datasets means that number statistics starts to lose its spot as number one source of uncertainty in galaxy evolution studies. With the availability of large wide field galaxy surveys as the Sloan Digital Sky Survey (SDSS York et al. 2000) or 2dF Galaxy Redshift Survey, and the deep, space based high resolution projects like the Hubble Ultra Deep Field, GOODS, GEMS and STAGES projects and the Cosmic Evolution Survey (COSMOS) with their 10^4 to 10^6 galaxies, other error sources become vital to understand.

If we want to understand the buildup of galaxies with their intricately linked evolution in stellar and black hole mass, luminosities, colors, morphological types, and the alternations between interaction and relaxation, we have to understand what the tools we apply really measure. Any given galaxy will look different when viewed with different instruments or when located at different redshifts, due to cosmological dimming and changes in rest-frame bandpass.

This makes the qualitative or quantitative classification of e.g. galaxy morphology non-trivial to compare for different redshifts or filters. As one example faint disks visible at one redshift will fade from the observer’s view at larger distances, not only affecting eyeball-classifications of morphology but also automatic

classifier software. Moreover, low surface brightness signs of interaction and structures, such as bars which are not prominent in the rest-frame ultraviolet, will not be visible at higher redshifts.

If the evolution of galaxies is to be studied via merger statistics, morphology-segregated evolution, star formation histories, and type-specific luminosity functions, all morphological classifiers have to be calibrated to deliver comparisons of similar quantities at all redshifts, taking into account bandpass-dependent properties and changes in signal-to-noise ratio.

From the analysis of HST survey data we know that the average surface brightness of the disc galaxy population fades with time (e.g. Lilly et al. 1998; Barden et al. 2005). The change is approximately 1-1.5mag depending on rest-frame bandpass over the redshift interval $0 < z < 1$. To some degree this surface brightness evolution counters the cosmological dimming and helps detecting low surface brightness features. Thus, if this effect is not taken into account, predictions about the recoverability of structural parameters or classifications are overly pessimistic.

For a few projects in the past, codes were created that would include some of these effects for specific applications or datasets (e.g. Abraham et al. 1996a,b; Giavalisco et al. 1996; Bouwens et al. 1998; Takamiya 1999; Burgarella et al. 2001; Kuchinski et al. 2001; van den Bergh et al. 2002; Lisker et al. 2006). However, to our knowledge no codes or datasets that include geometrical and cosmological bandpass shifting effects are currently publicly available. In the present article we describe the creation of artificial image data sets in the range $0.1 < z < 1.1$, computed from low- z SDSS galaxies

Electronic address: marco.barden@uibk.ac.at, jahnke@mpia.de, boris@mpia.de

¹ Max-Planck-Institut für Astronomie, Königstuhl 17, D-69117 Heidelberg, Germany

² Institute of Astro- and Particle Physics, University of Innsbruck, Technikerstraße 25, A-6020 Innsbruck, Austria

by artificial “redshifting”. Since we refrain from adding any evolutionary models but purely apply cosmological changes in angular size, surface brightness and filter bandpass, this dataset shows exactly how such galaxies will appear when observed from cosmological distances, at which redshift certain features become undetectable, and any quantitative classifier procedure can be tested for dependency on redshift effects.

Our code FERENGI, “Full and Efficient Redshifting of Ensembles of Nearby Galaxy Images”, and the present datasets were originally created for the morphological classification of active and inactive galaxies in the GEMS (Rix et al. 2004), STAGES (Gray & STAGES 2007), and COSMOS (Scoville et al. 2006) projects. The datasets for the HST ACS image characteristics of the GEMS and COSMOS project are freely available from our website³. As many studies might benefit from such data we also make the FERENGI code available on the same webpage for others to use with different input samples, redshifts, and instrument characteristics.

In the following we describe the input data in Section 2, the redshifting procedure including the basic cosmological formulae that enter, and the bandpass shift in Section 3, and the creation of realistic images from this information in Section 4 including example results (Section 5). Next, we present a series of tests characterising the robustness and accuracy of the code (Section 6). In Section 7 we discuss limitations of this procedure.

All examples and cosmology-dependent numbers given here are computed assuming a flat universe with $\Omega_\Lambda = 0.7$ and $h = H_0/(100 \text{ km s}^{-1} \text{ Mpc}^{-1}) = 0.7$.

2. INPUT GALAXY SAMPLE

The basic idea is to convert images of well resolved, low-redshift galaxies to images simulating the same galaxies at higher redshift. Input and output images can differ in assumed redshift, pixel size, point spread function (PSF) and noise properties. We explicitly compute two versions, with and without luminosity / surface brightness evolution terms. When purely considering instrumental and cosmological effects, users of such datasets can apply his or her tools to the exactly same galaxies, only located at different redshifts for calibration purposes. When including evolution, more realistic galaxies are created. For the current study we have implemented a linear scaling with redshift to make sources brighter at high redshift.

For this project we require input galaxy data with two main properties: i) Sufficient sampling: The combination of distance to the galaxy, pixel size and width of the PSF must be sufficient for the target pixel size and PSF width at the lowest target redshift (e.g. $z \geq 0.1$). ii) Information about the spectral energy distribution: The task needs homogeneous multiband imaging used for interpolation between filters to compute fluxes in the target filter band at the desired redshift without extrapolation.

The best source for such data are nearby galaxies from the SDSS. This survey provides imaging data in its own u , g , r , i , z filters with $0''.396/\text{pixel}$ sampling. We compute the maximum distance for input galaxies from the two requirement to i) simulate images with $0''.05$ and

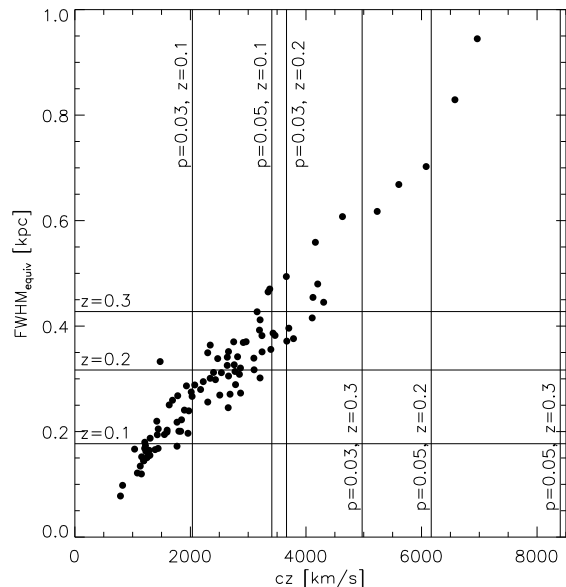


FIG. 1.— Sample selection. Shown is the width of the PSF of initially selected SDSS galaxies as a function of recession velocity. We give the width in equivalent linear dimensions, i.e. the linear size of the angular FWHM-width of the PSF in the SDSS r -band, at the distance of the galaxy. The horizontal lines correspond to upper selection limits for the input width to not exceed the ACS PSF width in the output images, at $z = 0.1, 0.2$ and 0.3 , respectively. The vertical lines mark the cz upper selection limits from input pixel size, to not exceed the output pixel sizes of $0''.03$ and $0''.05$ at the given redshifts.

$0''.03$ pixel size at a minimum redshift of $z = 0.1$, and ii) to have an output PSF not already broader than the $\sim 0''.096$ (FWHM) PSF of the ACS WFC drizzled images in the F606W or F814W filters. Figure 1 shows the resulting limit in cz and the limit from the width of the PSF for a sample of SDSS galaxies and their PSF conditions. Both criteria select a similar set of galaxies, corresponding to limiting recession velocities of $v \lesssim 2000, 3700$ and 5000 km s^{-1} for $z_{\text{out,min}} = 0.1, 0.2$ and 0.3 , respectively, and $0''.03$ output pixel size. For pixel size $0''.05$ the limits change to $v \lesssim 3400, 6200$ and 8400 km s^{-1} .

These technical aspects define the boundary conditions of our sample selection. We emphasise that at this point we do not aim to select a sample that is complete or representative for the general population of galaxies in a statistical sense. The sample selection only intends to span a large range of morphological types and common features, targeting large, rather luminous galaxies that could still be observed at larger z .

With this intention we make a selection of galaxies from the SDSS survey area, via the HyperLeda (Paturel et al. 1989; Prugniel & Heraudeau 1998) catalogue facility, with the following parameters: recession velocity $200 \leq v_{\text{vir}} \leq 7000$ corrected for Virgo infall (208 km s^{-1}), apparent isophotal diameter $D_{25} \geq 1$ arcmin, and apparent magnitude $B_T \leq 16$, and added a total B -band magnitude cut at $M_{B_T} \leq -19.5$.

Images were taken from the data release 4 (DR4) of the SDSS (Abazajian et al. 2005). As the SDSS imaging data is not targeted on individual galaxies, a fraction of about 40% of the selected galaxies extends beyond the borders of the $680 \times 590 \text{ arcsec}^2$ SDSS field of view. We excluded such galaxies as input after visual inspection.

In total we selected a sample of 96 galaxies with $cz < 7000 \text{ km s}^{-1}$ and very heterogeneous morpholo-

³ Website for retrieval of simulated datasets and the code FERENGI: <http://www.mpia.de/FERENGI/>

TABLE 1
DISTRIBUTION OF RC3 MORPHOLOGICAL CLASSES.

Class ^a	Number of galaxies
E	5
S0	8
early S ^b	16
late S ^c	40
Irr	5
pec ^d	22

^aCoded revised Hubble type according to RC3

^bHubble types S0/a–Sb

^cHubble types Sbc–Sm

^dmanually classified (multiple source and/or merger signatures)

gies. Figure 2 shows the Hubble diagram of the input sample. In the same figure and in Table 1 we give the distribution of morphological classification according to the *Third Reference Catalogue of Bright Galaxies* (RC3, de Vaucouleurs et al. 1991) to illustrate the sample composition. Note, that the class “peculiar” was manually selected for showing signs of ongoing mergers, or close or overlapping galaxies.

As in the local universe few galaxies show strong signs of interactions or even mergers, we gradually extended our selection range from $500 < cz < 3000$ out to $cz < 7000$. At larger distances we only included “peculiar”-looking sources like strong interactions or mergers. However, we also included some unrelated objects that have small projected radii or even overlap. Our intention here was to demonstrate the increasing difficulty at high redshift to morphologically discern interaction from projection effects.

3. REDSHIFTING PROCEDURE

The FERENGI redshifting procedure has two components, cosmological angular size and surface brightness changes on one side and bandpass shifting on the other. After computation of these cosmological effects we correct for PSF effects and add noise.

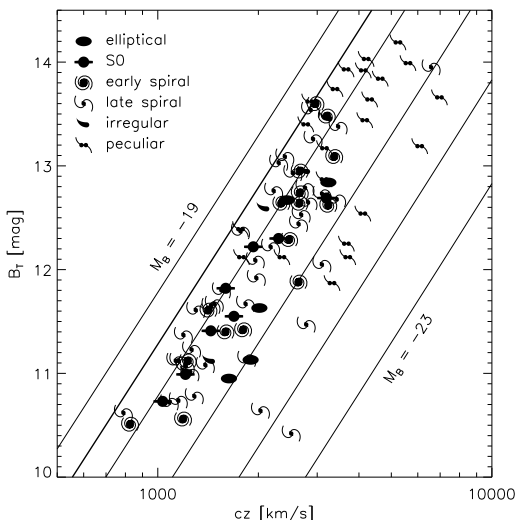


FIG. 2.— Hubble diagram of the selected input sample. Indicated are the approximate morphologies to give an overview over the diversity of the sample. The thin diagonal lines correspond to approximate absolute magnitudes M_B of -18 to -23 , spaced at 1 mag interval. The thick lines is our imposed selection cut at $M_B = -19.5$.

3.1. Angular size and surface brightness

When converting from an input image with pixel size p_i of a galaxy at redshift z_i to an output redshift z_o and desired pixel size p_o both angular sizes and surface brightnesses have to be modified for distance and cosmological effects. Using $\tan(a) \simeq a$ for small angles, the angular size a of a given linear dimension changes as

$$\frac{a_o}{a_i} = \frac{d_i/(1+z_i)^2}{d_o/(1+z_o)^2}$$

with the luminosity distance d . Since the input image will be rebinned to the output pixel size, angular sizes in units of pixels n , and thus image rebinning factors, are

$$\frac{n_o}{n_i} = \frac{d_i/(1+z_i)^2}{d_o/(1+z_o)^2} \frac{p_i}{p_o}. \quad (1)$$

The flux in each pixel is subject to surface brightness dimming. If we require the galaxy absolute magnitude to be conserved

$$M = m_i - 5 \log(d_i) - c = m_o - 5 \log(d_o) - c$$

we find a relation for the ratio of observed fluxes f of the in- and output images

$$2.5 \log \left(\frac{f_o}{f_i} \right) = m_i - m_o = 5 \log \left(\frac{d_i}{d_o} \right) \Leftrightarrow \frac{f_o}{f_i} = \left(\frac{d_i}{d_o} \right)^2, \quad (2)$$

which gives the standard bolometric surface brightness dependence of $(1+z)^{-4}$. The finite filter width is taken care of in the next component.

Note, that in order to account for the bandpass shift it is imperative to match object positions in the input images. This matching is a complex process, which potentially includes shifting, rotation and scaling of the input data. Moreover, the PSFs of the data should match. In the case of strongly varying PSFs colour terms may be introduced in the bandpass shifting. When combining e.g. GALEX and SDSS data, to extend the wavelength baseline to the UV, the users would have to prepare the input image accordingly. They have to shift all images to a common position, scale the GALEX image to the SDSS pixel scale, possibly rotate the GALEX image to match the SDSS frame and smooth all SDSS images to the GALEX FWHM. The so-processed images are then input to FERENGI. Thus, preparing the input appropriately, FERENGI is not limited in the combination of telescopes, filters, or instruments.

3.2. Bandpass shift

While the above rebinning and flux rescaling takes care of all geometrical effects, bandpass shifting and stretching still has to be added. The cosmological redshift (by definition) shift the observed restframe bandpass for a given observing filter as a function of redshift as well as change the size of a given filter. In addition we want to have the option to produce images for a range of optical observed filters.

For this task we input spectral information in the form of multiband imaging. A combination of observers filter and redshift defines the desired rest-frame filter curve. For each pixel of the input frame we calculate the expected flux for this rest-frame filter, by interpolating between multiband information on this pixel. This task

is facilitated by the routine `k_correct` (v4.14, Blanton et al. 2003, available for IDL and C) that was written to fit spectral templates to a set of multiband images. We use `k_correct` to determine a best template for individual pixels in an image, and from this the flux in each pixel for a given filter. We so construct a rest-frame filter image. This bandpass shift and the above size-rebinning are interchangeable in order. To minimize the computational effort and to reduce noise we first recomputed the (coarser) redshifted images and then applied the bandpass shift. Also, only pixels with flux exceeding 2 times the rms of the background are input to `k_correct` (optional feature). The remaining pixels receive a flux-weighted K -correction computed from the bright pixels. While this could become more important at low S/N levels, it showed not to have a significant effect for the currently chosen bright sample of galaxies.

Note, the template set incorporated in `k_correct` stems from (Bruzual & Charlot 2003) models. These model templates cover the rest-frame wavelength range from UV to IR (600Å to 320μm). As long as the input filters together with the targeted output redshift fall within this range any combination is possible.

4. POINT SPREAD FUNCTION AND NOISE

Two essential ingredients for realistic images are i) to mimic the resolution of the real data by convolution with an appropriate PSF and ii) to generate realistic noise levels for galaxy and background.

The input SDSS galaxies were observed under varying seeing conditions with an average PSF width of 1''.4 FWHM corresponding to ~ 3.5 SDSS camera pixel. After application of the redshifting procedure the intrinsic PSF is of finite width and non-negligible. While for point- or composite sources as type I AGN the detailed knowledge about the PSF is essential, the requirements are not so stringent for extended galaxies. However, as the simulated dataset is meant to calibrate quantitative morphological analysis methods and programs, it is important to create a PSF that is sufficiently similar to the real PSF for the task in question.

In light of this we attempt to reach a final PSF as close as possible in shape and width to the ACS PSF in the desired band. This involves the creation of a convolution kernel that will produce the ACS PSF shape from the input PSF shape. As the width and geometric shrinking of the PSF depends both on input and target redshift, and the input PSF varies, this kernel needs to be recomputed for each input galaxy and output redshift. This is done by a transformation into Fourier space, suppression of noise by Wiener filtering, and subsequent division of the spectra of the two PSFs. After transformation of this quotient back into the spatial domain we receive the function that is needed to convolve the input image to reach a PSF close to the ACS PSF. This is mathematically equivalent to a deconvolution of the output PSF with the desired input PSF. For the comparably high S/N PSF in these data this works fairly well. Note, that the filter of the input PSF is chosen from the set of SDSS filters minimising the wavelength difference to the desired rest-frame band, thus also minimising colour gradients in the reconstructed PSF. However the seeing is wavelength dependent and can also vary on the short timescales between the integration in the different SDSS filter bands.

This can still result in small differences between the actual PSF present for a reconstructed galaxy image and the reconstructed PSF image. In order to remove this wavelength dependency we choose a well sampled, not saturated star in each SDSS filter as PSF. We convolve the SDSS images with a kernel (as described above) that generates a round Gaussian PSF with a FWHM for all filters of $1.1 \times$ the largest extent of the input PSFs. Thus, PSF resolution effects and colour gradients are kept at an absolute minimum. A comparison of the reconstructed and target ACS PSF shows a difference of less than 0.1% in each individual pixel.

This procedure is limited to cases where the widths of in- and output PSF are sufficiently different. If not, noise will introduce artifacts as ringing patterns or mathematical ghost images near bright sources, which is clearly not desirable. This occurs primarily when the input PSF resolution becomes comparable to the output PSF width – so the convolution function becomes very narrow – i.e. at the low redshift end.

In order to facilitate proper modelling of the redshifted galaxy images we discourage the use of the publicly available GEMS or COSMOS PSF, but suggest to prefer the reconstructed PSF instead. Although this might not be crucial for determining two-dimensional galaxy light profiles, it might make a significant difference in the case of AGNs and their host galaxies. Likewise, we recommend using scaled versions of the reconstructed PSF to be put on top of redshifted galaxy images in order to create artificial AGNs.

Noise in the output images has two main sources, sky background and the galaxy flux itself. For one-orbit exposures as for COSMOS and GEMS the sky background noise dominates over the readout noise ($\sim 5.2 e^-$ for the ACS Wide-Field Camera) after a few 100 seconds of integration, in the case of broad band filters. Thus the latter is negligible. Also, at $0.0022 e^- s^{-1}$ the ACS/WFC dark current does not play a significant role.

The background noise in our simulations is not created from random numbers, but the noise-added galaxy images are added onto blank sky taken from the observed data itself (for ACS data reduction for GEMS and COSMOS see Caldwell et al. 2006; Koekemoer et al. 2006). In this way reduction signatures like correlated noise and intrinsic small variations in the otherwise empty regions of the sky are also present in the simulated data. We extract several 60'' square fields from the data. While we choose comparably empty regions of the sky, the ACS camera is so efficient over one orbit for both the COSMOS and GEMS filters that there exists no “empty” sky over more than 10–20'' regions. To remove prominent remaining objects we replace the corresponding pixel regions with unique other small patches of blank sky. This process does not involve any filtering, only replacing. In this way the resulting empty sky fields are very good random representations of empty sky regions. If for an application the sensitivity of a measurement to small residual back-/foreground objects is to be tested, the user can add his/her favorite contamination or even use random patches of uncleaned sky as background.

Noise has to be added also to the redshifted galaxy images themselves. The S/N per pixel of the input galaxies is high by definition of the sample. After redshifting and PSF adaptation their photon noise is negligible compared

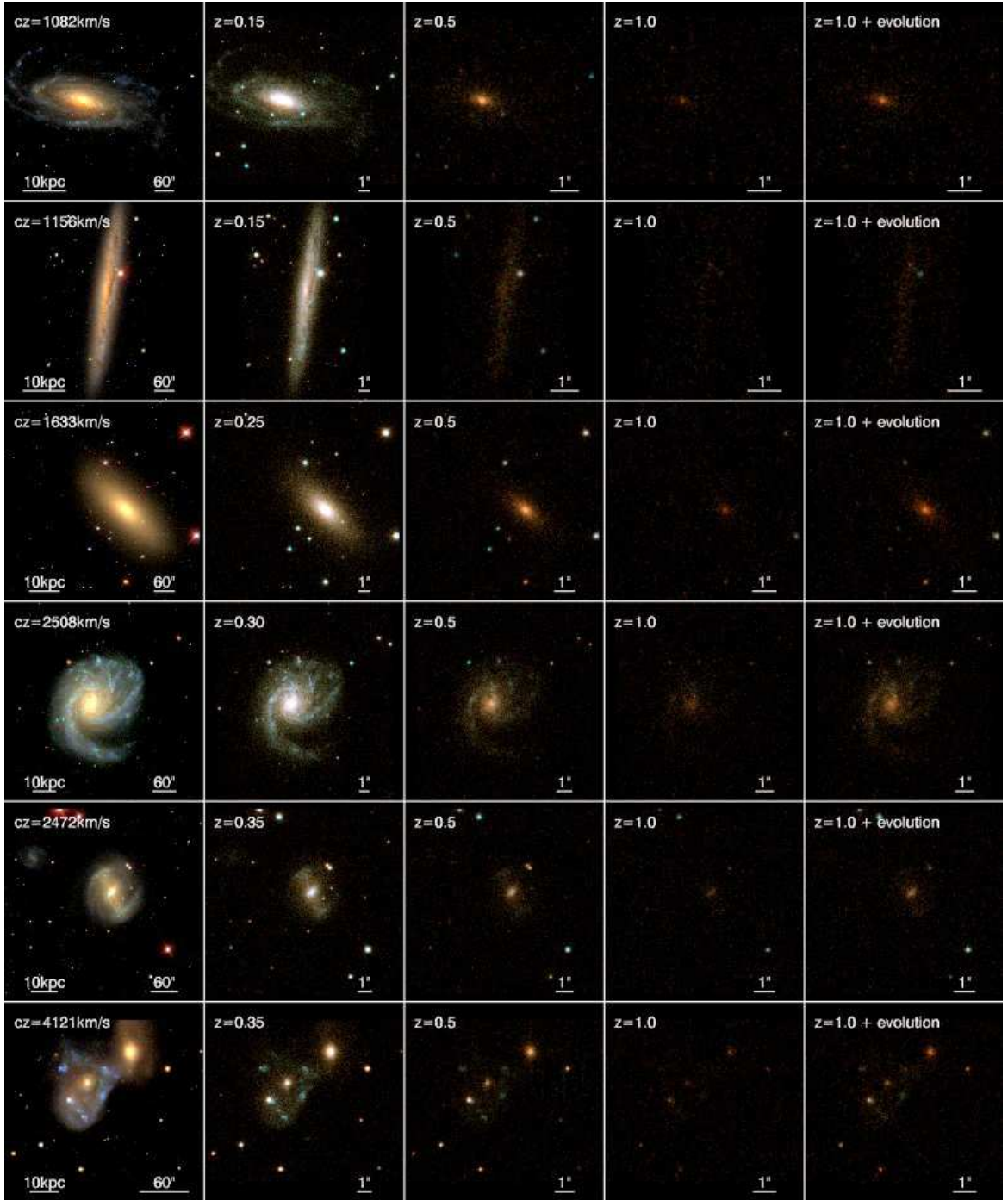


FIG. 3.— Redshifting examples. From left to right the first four panels in each row show the original SDSS *gri*-colour composite image and the redshifted GEMS F606W-F814W false colour images at $z = 0.15 - 0.45, 0.5, 1.0$. The fifth column includes magnitude evolution by $\Delta m = -1 \times z$ mag at redshift $z = 1$. Apparent scales are indicated in each panel; physical scales are the same in each panel and therefore only marked in the leftmost panel.

to the noise expected from a single orbit HST ACS exposure. The resulting images are scaled in flux corresponding to e.g. 2028 seconds (COSMOS) integration time, in the respective output filter. The galaxy image – in units of electrons per pixel – then has random Poisson noise added, with a σ^2 corresponding to the galaxy flux per pixel. Subsequently, the galaxy is added on top of the empty background images. In a statistical sense this procedure is not strictly correct, as the photon noise addition should be applied to the sum of sky and galaxy, but can not be avoided if real sky images are to be used. How-

ever, the resulting higher noise only appears in regions of the final image where sky background and galaxy contribute equally in noise, so in the faint isophote regime of the galaxy.

5. RESULTING GALAXY IMAGES

Artificially redshifted galaxies are created for a redshift range out to $z = 1.1$. The starting redshift was taken for each galaxy either $z = 0.1$ or the minimum redshift at which both input PSF width and pixel size begin to match the output PSF and pixel size. We give images for

TABLE 2
REDSHIFTING TEST PROCEDURE.

No.	Task	Provides set of	Tests	Affected Bands	Fig.
0	fit real images using GALFIT	GALFIT parameters		u, g, r, i, z	-
1	from output of 0 create local smooth model images & fit	artificial SDSS galaxies	double-check with 0	u, g, r, i, z	-
2	create high- z smooth model images & fit	smooth model images at high- z	GALFIT response to decreasing S/N	u, g, r	5
3	redshifting of output from 1 (K -corr. disabled) & fit	redshifted, non- K -corrected smooth model images	impact of downscaling, PSF effects	u, g, r	6
4	redshifting of output from 1 (K -corr. enabled) & fit	fully redshifted, K -corrected smooth model images	impact of K -correction	ACS filter	7
5	redshifting of 0 & fit	redshifted real images	in comparison with 4, impact of morphology	ACS filter	8

steps of $\Delta z = 0.05$ out to $z = 0.5$ and $\Delta z = 0.1$ beyond that, thus a maximum of 15 output redshifts per input galaxy.

Simply shifting local galaxies out to high redshift makes them look rather faint in comparison to real average galaxies at such distances. In order to reflect the brightness increase of high redshift sources we put in a crude mechanism to introduce evolution. This optional feature allows to make galaxies brighter as a linear function of redshift:

$$M_{\text{evo}} = x \times z + M$$

Setting $x = -1$ would make a galaxy 1 mag brighter at redshift $z = 1$ as it would normally be. Yet, this option is not meant to be a substitute for real morphological or photometrical evolution and does not replace stellar evolution codes. The reason for putting in such a simple functional form is the application of galaxy classification by eye. If one is to re-identify galaxies shifted to high redshift, the task is made increasingly unfair compared to real galaxies, which on average do become brighter at higher redshift, if one does not apply artificial brightening.

A few resulting example images for COSMOS are shown in Figure 3. All images, for both GEMS and COSMOS are made available electronically.

6. TESTS OF FERENGI AND APPLICATION OF GALFIT

In order to demonstrate the accuracy of FERENGI and characterise its limits, we perform a number of tests. We use the programme GALFIT (Peng et al. 2002) to determine structural parameters, which is often used for parameter estimation and morphological classification of galaxy samples, particularly in survey applications. The programme is (potentially) susceptible to S/N changes and morphological K -correction, like any other fitting code. Yet, Häußler et al. (2007) have shown that GALFIT is very robust and does not exhibit systematic biases when fitting radial surface brightness models to artificial 2d Sérsic-type⁴ light profiles. In the following section we make use of this robustness and apply GALFIT to various sets of simulated 2d Sérsic profiles to determine the dependence of structural parameters on the application of FERENGI.

⁴ The Sérsic profile is a generalized exponential profile, with one parameter n . For $n = 1$ the profile is a simple exponential curve, typical of disc galaxies, for $n = 4$ the profile becomes a de Vaucouleurs exponential $r^{1/4}$ profile.

In addition to GALFIT we use a code described in Häußler et al. (2007) to create 2d Sérsic profiles mimicking our observed galaxies. This procedure features a fine subsampling of the inner pixels allowing highly accurate flux calibration. Convolution is done with the original PSF as reconstructed from the SDSS, after smoothing the individual five bands to a round Gaussian configuration. Poisson noise and a real SDSS sky background image are added. Such simulated images are created for all five SDSS bands u, g, r, i, z .

6.1. Procedure for individual galaxies

We conduct the simulations in six different steps to check for possible systematics introduced at each step. The summary of each step is shown in Table 2. We show by way of illustration an example of an elliptical galaxy (Fig. 4). It has an almost de Vaucouleurs-type light profile (n increases from 3.2 to 3.6 going from u to r band). The size of the galaxy is constant across the three bands; the magnitude covers a range of over 2.5 magnitudes – u being faintest and r brightest, as expected for a red elliptical.

- We start by using GALFIT to fit a Sérsic profile to the set of SDSS images belonging to the objects. This provides the basis for simulating the smooth model images.

- With the GALFIT parameters we create artificial model images using the procedure by Häußler et al. (2007) described above, resembling smooth versions of the SDSS galaxy images. A fit to these smooth images in all bands confirms the stability of the process by retrieving almost exactly the input values.

- Next we create artificial model images of the same galaxies, as they would appear at high redshift (our set of output redshifts given in Section 5) using the parameters from before, in the u, g , and r bands. We do not apply FERENGI here, but only convert the linear scales according to redshift. This will quantify the response of GALFIT to the decreasing S/N as a result of cosmological surface brightness dimming.

Figure 5 demonstrates how GALFIT performs as a function of redshift for the example galaxy (No. 2 from Table 2). The higher the redshift, the lower is the S/N of the object and its surface brightness. Quite expectedly, the quality of the recovered fit parameters degrades with redshift. As the u -band has the lowest S/N of all SDSS filters, GALFIT fares worst there; r -band behaves best, having the highest S/N. The chosen galaxy being rather red, this effect is even amplified. As the galaxy is rather bright, overall, the deviations in the parameters

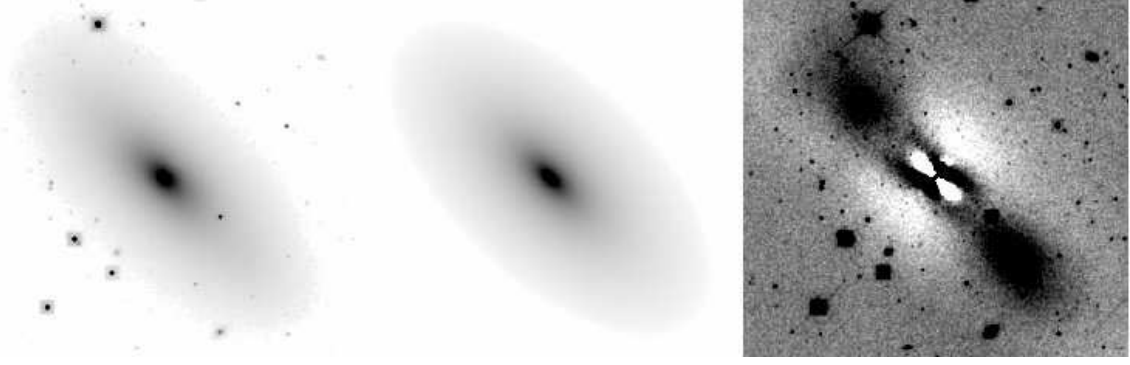


FIG. 4.— Example galaxy for testing FERENGI. Original SDSS r -band image (left); GALFIT model image (middle); residual image (SDSS minus GALFIT model; right). The differences in the residual image are $\sim 15\%$ in the inner and 2-3% in the outer regions (with respect to the flux in the original image).

from their input values are rather small. In order to allow a comparison with GEMS, we compute the average apparent surface brightness of our sample galaxies with $3 < n < 5$ in u , g and r . From Häußler et al. (2007) we obtain the corresponding GALFIT errors in GEMS. The results are listed in Table 3.

- Now we use FERENGI on the simulated smooth u , g , and r band model images to create versions of these images appropriate for higher redshifts. The Sérsic fits to this set of images we use to determine the influence of conversion to a new pixel grid and related PSF on different galaxy parameters, as a function of redshift. Note that the K -correction code is *disabled* for this purpose. The image set contains the flux of the SDSS filters transformed to a new pixel size, PSF, background noise properties and the cosmological effect of surface brightness dimming.

For the example galaxy the left hand side of Figure 6 shows the same as Figure 5; the right hand side has the values from Figure 5 subtracted in order to indicate the extra influence of the re-gridding process. We find no additional systematics and the scatter hardly increases.

- After that we *enable* K -correction, thus fitting an SED to all five SDSS bands and extracting the flux at the position of the observed ACS filter, in addition to the down-scaling and surface brightness dimming. This provides a set of images representing the simulated SDSS galaxies as they would look at high redshift including all cosmological effects (No. 4 from Table 2).

The result for the example galaxy is shown in Figure 7. In the top panels we plot the original input values.

TABLE 3
STATISTICAL ERRORS FROM GEMS.

z	Band	M [mag]	R_e [%]	n [%]
0.2	u	0.05 ± 0.42	-0.06 ± 0.41	-0.03 ± 0.27
	g	0.01 ± 0.15	0.00 ± 0.22	-0.01 ± 0.21
	r	0.01 ± 0.13	0.00 ± 0.20	-0.01 ± 0.20
0.4	u	0.10 ± 0.50	-0.08 ± 0.48	-0.05 ± 0.28
	g	0.02 ± 0.20	-0.01 ± 0.27	-0.01 ± 0.22
	r	0.01 ± 0.17	0.00 ± 0.24	-0.01 ± 0.21
0.8	u	0.18 ± 0.61	-0.15 ± 0.50	-0.06 ± 0.31
	g	0.03 ± 0.32	-0.04 ± 0.35	-0.02 ± 0.26
	r	0.02 ± 0.27	-0.03 ± 0.32	-0.02 ± 0.25

The morphological parameters of the average galaxy with $3 < n < 5$ in our sample are: $M = [-19.53, -21.09, -21.95]$, $R_e = [12.0, 7.7, 9.9]$ in $[u, g, r]$. Indicated errors are 1σ standard deviations from the mean.

Also shown are the fit values from using the K -correction code. In order to provide a rough estimate of the deviation from the expected values we fit the five values from the simulated SDSS images with a polynomial and subtract this fit. Going into all the details of modelling galaxy photometry and structure in multiple wavebands (or even continuously) is well beyond the scope of this paper. Therefore, we regard the lower panel not as a proper estimate of the error budget, but rather an indication of systematic trends. Points missing from the lower panel were left out in order not to overstretch the plotting axis and to focus on the main region of interest.

- Finally, we run FERENGI on the real SDSS images including K -corrections (No. 5 from Table 2). The GALFIT results for this series reveals in comparison to the redshifted simulations (No. 4 from Table 2) the impact of morphology on the whole process (see Figure 8).

As the performed calculations are virtually identical any differences in the output must result from irregularities in the real data, such as tidal features, spiral arms, dust lanes, etc. The example galaxy was chosen to

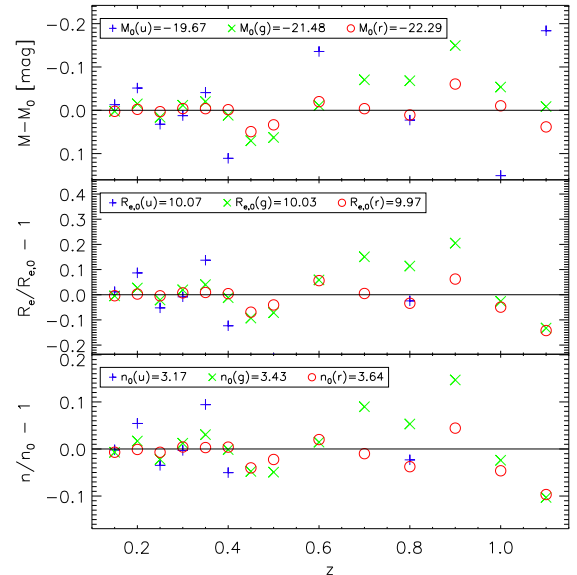


FIG. 5.— The GALFIT error from fitting simulated images for an example galaxy. Top panel: absolute magnitude difference; middle panel: ratio of measured and input half-light radius; bottom panel: ratio of measured and input Sérsic index. Pluses, crosses and circles show u -, g - and r -band, respectively. Boxes in each panel indicate the absolute quantities of the simulation input: absolute magnitude, physical half-light radius in kpc and Sérsic index.

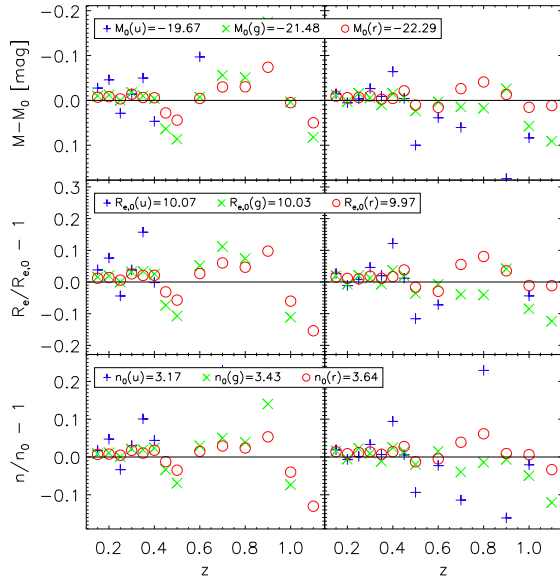


FIG. 6.— Performance of FERENGI (for an example galaxy) – K -correction disabled. Same axes as in Figure 5. Left panel: difference of simulated parameters and output after redshifting without applying K -corrections. Right panel: same as left panel minus the offsets from Figure 5, thus indicating the additional error implied by re-gridding, PSF-resampling and changed noise properties.

be rather featureless. Therefore, a perfect match is obtained. Yet, in the majority of cases we find systematic differences: Either redshift dependent deviations (originating from irregularities) or global shifts towards higher or lower values. At the highest redshift ($z \sim 1$) the impact of morphology might decrease again as virtually all features are smeared out.

Yet, the reason for global offsets is of technical nature: the drastic change in resolution and depth when transforming a low redshift image (cz of a few thousand km/h) to high redshift ($z \gtrsim 0.1$) results in the rebinned PSF not being Nyquist sampled any more. This causes shifts when performing Fourier transformations. The effect is more pronounced at low ($z \gtrsim 0.1$) than at high ($z \sim 1$) redshift, because eventually the PSF becomes pointlike.

6.2. Average results

We applied FERENGI to all 96 sample galaxies. This allows us to quantify systematic biases of the redshifting code in some detail. In Figure 9 we show the average deviation from the input values for simulations of high redshift galaxies and downsampled versions of simulated galaxies (No. 2 & 3 from Table 2). The errors and systematic offsets are not significantly different. For the given observational setup (redshifting of SDSS images to COSMOS and GEMS) roughly at $z \sim 0.7$ larger deviations in particular in u -band occur. Note, that these departures from the expected mean are seen in the simulated images as well. Therefore, they must originate from the specific GALFIT setup, but not FERENGI itself.

In order to compare the results of the high redshift simulations and the downscaling-only simulations (No. 2 & 3 from Table 2) with the K -corrections-enabled setup (No. 4), we plot as a function of redshift the measurements in the SDSS filters closest to the rest-frame ACS filter (Figure 10). Interestingly, the error bars in the right panel of Figure 10 (No. 4) at the highest two red-

shift bins are *smaller* than without K -corrections (No. 3) or even in the pure simulations (No. 2). The reason for this is, that the SED fitting uses all five SDSS bands and therefore introduces some information extrapolated from g , r , i and z (the closer bands being weighted more strongly than the redder bands) to improve the low S/N u -band data. However, this implies also that template mismatches might change the morphological appearance of the object to some extent. As the SED-fitting code is deeply embedded in `kcorrect` we do not attempt to characterise the impact any further. Moreover, we find, that the K -correction code on average introduces stronger fluctuations and increases the error bars slightly at lower redshifts. Systematic deviations to lower brightnesses, radii or Sérsic indices are not statistically significant.

7. DISCUSSION AND CONCLUSIONS

We take from Figures 9 and 10 that FERENGI has no unwanted systematic effects on measured morphological and photometrical parameters of simulated galaxies. The deviations from theoretical values are well within the uncertainties expected from, in this case, GALFIT, also in absolute terms. Both linear scales as well as magnitudes are well reproduced. This includes the band-pass shifts induced by redshifting and different filters, as is demonstrated in the right panels in Figures 10: The `kcorrect` module correctly interpolates between input filter images. We cannot exclude issues when *extrapolating* `kcorrect` templates, but we explicitly restrict the output range of redshifts to only use template *interpolation*, between bands.

We make FERENGI publically available from our webpage, as are redshifted sets of images for redshifts $0.1 \leq z \leq 1.1$ and different HST ACS filters. Primarily these are created for the GEMS (F606W and F850LP at $0''.03/\text{pixel}$) and COSMOS (F814W at $0''.05/\text{pixel}$) projects, but the code can be modified and used for other filters. The user can extend the input sample of images (also provided on the webpage), to other objects, filter curves, and output redshifts, and in principle also to other data sources. We leave it up to the user to update FERENGI with respect to the K -correction module when including other input filter bands.

As stated, templates are used for interpolation between input filters. They can theoretically also be extrapolated beyond the input wavelength interval, if one has faith in the templates. However, we strongly advise against this for a different reason: Due to the limited S/N available for the pixel-by-pixel K -correction that is computed, a mild extrapolation might be acceptable, but the noise of the output pixels and systematic deviations will obviously increase with distance to the last supported wavelength. As various templates might be degenerate when interpolating, there might be striking differences on extrapolation, resulting in large errors in the output flux.

As a second caveat we note that stars in the input images are not treated separately in FERENGI or in the provided datasets. *Any* flux in the input images, be it stars or back-/foreground galaxies, will be treated as if it were at the distance of the target and thus be redshifted. While distant background galaxies usually disappear, stars will be represented with the output PSF, resembling a faint dense star field (the density of stars

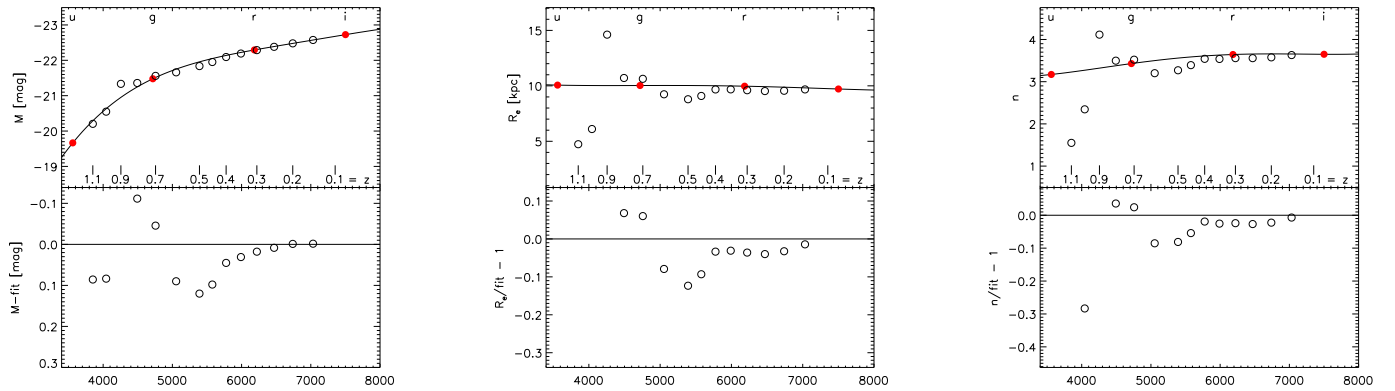


FIG. 7.— Performance of FERENGI (for an example galaxy) – K -correction *enabled*. Top panels: Turning on K -corrections we compare the absolute magnitudes, half-light radii and Sérsic indices of the simulated SDSS images (filled circles), which were used as input for the redshifting, directly with the redshifted output (open circles). The solid line marks a polynomial fit to the input data. Bottom panel: subtracting the polynomial fit from the output data.

is enhanced quadratically with decreasing linear scales as the simulation redshift increases). Of even greater concern are foreground (or closer background) galaxies. In the output, their physical properties are calculated falsely as their assumed distance is not correct. Whether the resulting images will in the end be reliable representations of reality, strongly depends on the quality of input images, the type of galaxies, and their correspondence with the templates used.

The authors gratefully acknowledge numerous helpful discussions with Chien Y. Peng and Hans-Walter Rix. This publication makes use of the Sloan Digital Sky Survey, <http://www.sdss.org>. We selected the SDSS

data using the HyperLeda database (<http://leda.univ-lyon1.fr/intro.html>). This work is also based on observations taken with the NASA/ESA *Hubble Space Telescope*, which is operated by AURA. Support for the GEMS project (<http://www.mpia.de/GEMS/gems.htm>) was provided by NASA through grant number HST-GO-9500. The HST COSMOS Treasury program was supported through NASA grant HST-GO-09822 (<http://cosmos.astro.caltech.edu>). M.B. was supported in part by the Austrian Science Foundation FWF under grant P18416. K.J. was supported by the German DLR under project number 50 OR 0404 and by the German DFG with grant SCHI 536/3-1 within the priority program 1177.

REFERENCES

- Abazajian, K., Adelman-McCarthy, J. K., Agüeros, M. A., Allam, S. S., Anderson, K. S. J., Anderson, S. F., Annis, J., Bahcall, N. A., Baldry, I. K., et al. 2005, *AJ*, 129, 1755
- Abraham, R. G., Tanvir, N. R., Santiago, B. X., Ellis, R. S., Glazebrook, K., & van den Bergh, S. 1996a, *MNRAS*, 279, L47
- Abraham, R. G., van den Bergh, S., Glazebrook, K., Ellis, R. S., Santiago, B. X., Surma, P., & Griffiths, R. E. 1996b, *ApJS*, 107, 1
- Barden, M., Rix, H.-W., Somerville, R. S., Bell, E. F., Häußler, B., Peng, C. Y., Borch, A., Beckwith, S. V. W., Caldwell, J. A. R., Heymans, C., Jahnke, K., Jogee, S., McIntosh, D. H., Meisenheimer, K., Sánchez, S. F., Wisotzki, L., & Wolf, C. 2005, *ApJ*, 635, 959
- Blanton, M. R., Brinkmann, J., Csabai, I., Doi, M., Eisenstein, D., Fukugita, M., Gunn, J. E., Hogg, D. W., & Schlegel, D. J. 2003, *AJ*, 125, 2348
- Bouwens, R., Broadhurst, T., & Silk, J. 1998, *ApJ*, 506, 557
- Bruzual, G. & Charlot, S. 2003, *MNRAS*, 344, 1000
- Burgarella, D., Buat, V., Donas, J., Milliard, B., & Chapelon, S. 2001, *A&A*, 369, 421
- Caldwell, J. et al. 2006, *PASP*, in prep.
- de Vaucouleurs, G., de Vaucouleurs, A., Corwin, H. G., Buta, R. J., Paturel, G., & Fouque, P. 1991, *Third Reference Catalogue of Bright Galaxies* (Volume 1-3, XII, 2069 pp. 7 figs.. Springer-Verlag Berlin Heidelberg New York)
- Giavalisco, M., Livio, M., Bohlin, R. C., Macchetto, F. D., & Stecher, T. P. 1996, *AJ*, 112, 369
- Gray, M. & STAGES. 2007, *MNRAS*, in prep.
- Häußler, B. et al. 2007, submitted to *ApJ*
- Koekemoer, A. et al. 2006, submitted to *ApJS*
- Kuchinski, L. E., Madore, B. F., Freedman, W. L., & Trehwella, M. 2001, *AJ*, 122, 729
- Lilly, S., Schade, D., Ellis, R., Le Fevre, O., Brinchmann, J., Tresse, L., Abraham, R., Hammer, F., Crampton, D., Colless, M., Glazebrook, K., Mallen-Ornelas, G., & Broadhurst, T. 1998, *ApJ*, 500, 75
- Lisker, T., Debattista, V. P., Ferreras, I., & Erwin, P. 2006, *MNRAS*, 370, 477
- Paturel, G., Fouque, P., Bottinelli, L., & Gouguenheim, L. 1989, *A&AS*, 80, 299
- Peng, C. Y., Ho, L. C., Impey, C. D., & Rix, H.-W. 2002, *AJ*, 124, 266
- Prugniel, P. & Heraudeau, P. 1998, *A&AS*, 128, 299
- Rix, H.-W., Barden, M., Beckwith, S. V. W., Bell, E. F., Borch, A., Caldwell, J. A. R., Häußler, B., Jahnke, K., Jogee, S., McIntosh, D. H., Meisenheimer, K., Peng, C. Y., Sánchez, S. F., Somerville, R. S., Wisotzki, L., & Wolf, C. 2004, *ApJS*, 152, 163
- Scoville, N. et al. 2006, submitted to *ApJS*
- Takamiya, M. 1999, *ApJS*, 122, 109
- van den Bergh, S., Abraham, R. G., Whyte, L. F., Merrifield, M. R., Eskridge, P. B., Frogel, J. A., & Pogge, R. 2002, *AJ*, 123, 2913
- York, D. G., Adelman, J., Anderson, J. E., Anderson, S. F., Annis, J., Bahcall, N. A., Bakken, J. A., Barkhouser, R., Bastian, S., et al. 2000, *AJ*, 120, 1579

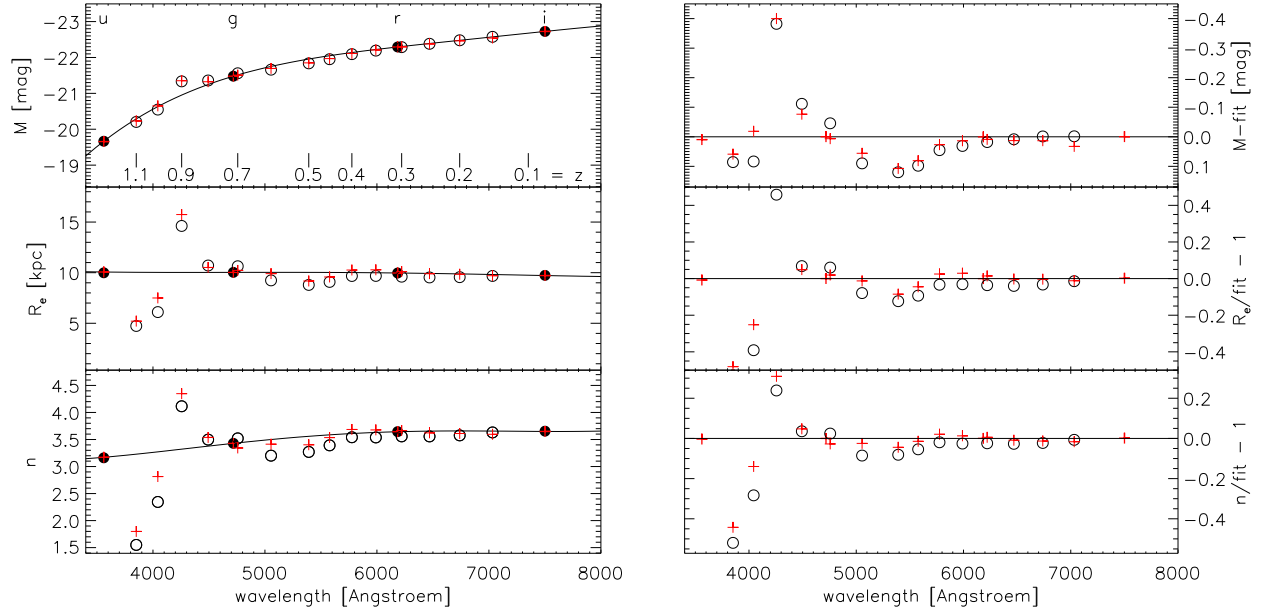


FIG. 8.— Comparison of reality and simulation (for an example galaxy). Plots for magnitude, half-light radius and Sérsic index from top to bottom. Simulated data shown as circles; real data as pluses. Thick / filled symbols indicate local input data. Left: absolute quantities. The solid line shows a polynomial fit to the simulated data. Right: polynomial fit subtracted from the data. Hardly any difference is visible, indicating that the input galaxy fits well the featureless Sérsic profile.

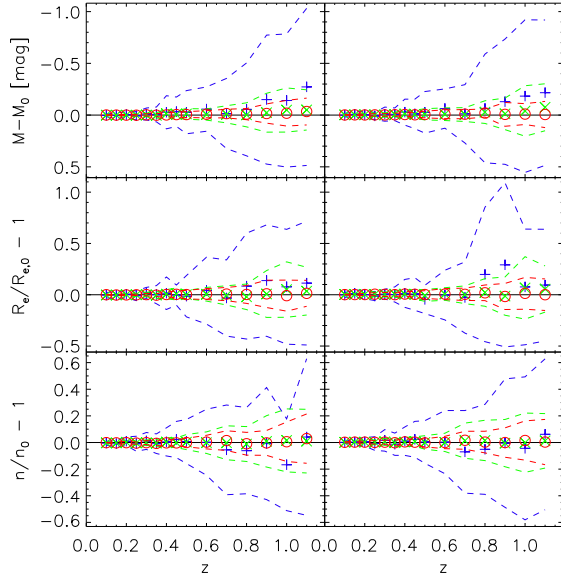


FIG. 9.— Average deviations from the input values (mean values for the whole sample). Left: simulating synthetic galaxies at various redshifts. Right: applying FERENGI to simulated SDSS galaxies without K -correction. From top to bottom: absolute magnitude difference, ratio of measured and input half-light radius, ratio of measured and input Sérsic index. Pluses, crosses and circles symbolise u -, g - and r -band, respectively. The error bars are robust 1σ standard deviations from the mean.

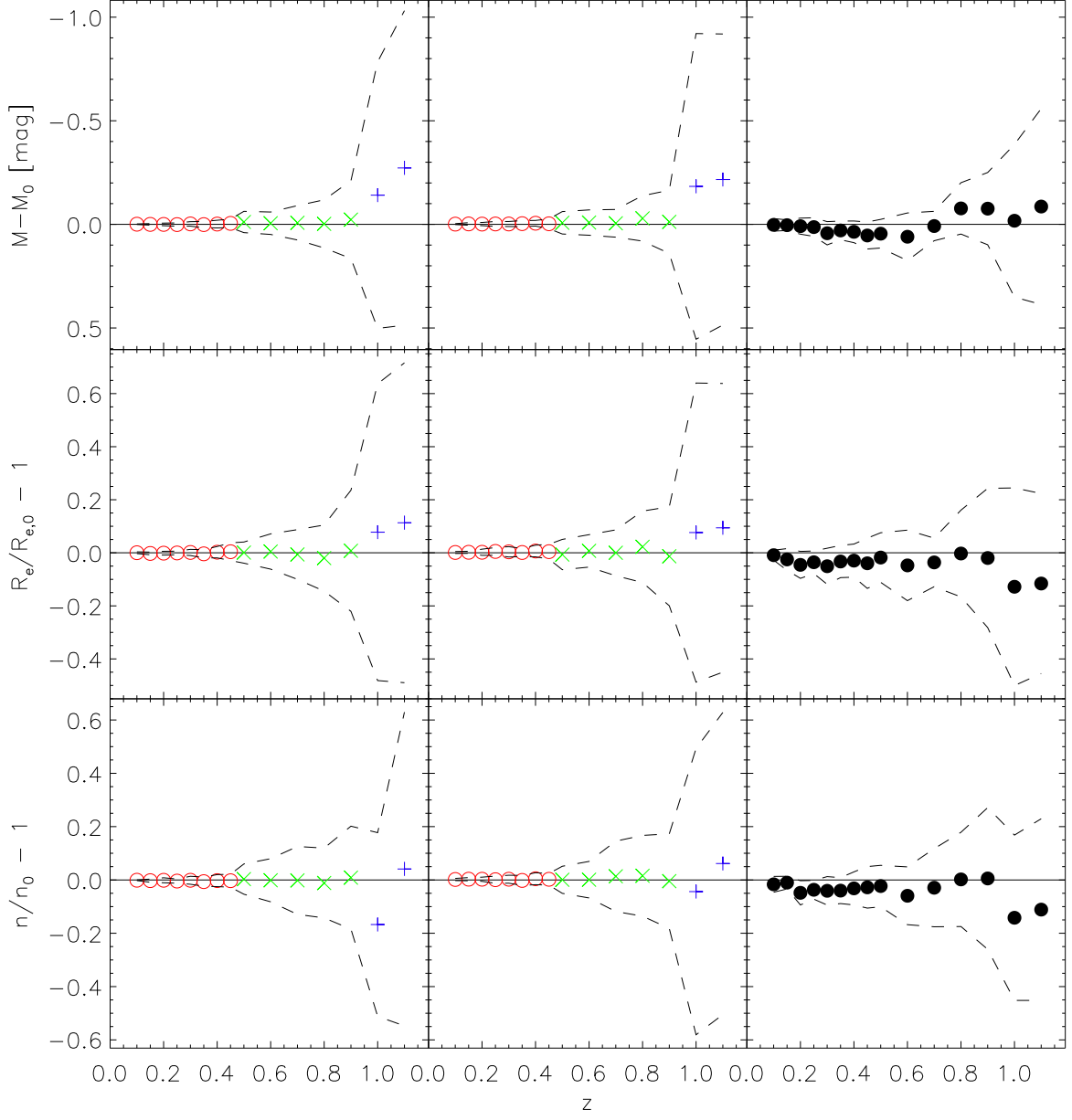


FIG. 10.— Average deviations from the input values including K -corrections. Panel lines show absolute magnitude difference, ratio of measured and input half-light radius and Sérsic index; panel columns show simulation of high redshift galaxies, redshifting of simulated galaxies without K -corrections and redshifting of simulated galaxies with K -correction enabled (No. 2, 3 & 4 of Table 2, respectively). The error bars are robust 1σ standard deviations from the mean. The leftmost two panel columns show data from Figure 9. In contrast to Figure 9, we choose to plot at each redshift the SDSS band closest to the rest-frame of the ACS filter ($z \geq 1$: u -band – pluses; $0.5 \leq z \leq 0.9$: g -band – crosses; $z \leq 0.45$: r -band – circles).